



CrossMark
click for updates

Cite this: *RSC Adv.*, 2015, 5, 54364

Synergistic effect in bimetallic copper–silver (Cu_xAg) nanoparticles enhances silicon conversion in Rochow reaction†

Zailei Zhang,^{*a} Yongjun Ji,^a Jing Li,^a Ziyi Zhong^b and Fabing Su^{*a}

The oleylamine thermal reduction process was employed to prepare bimetallic copper–silver (Cu_xAg ($0 \leq x \leq 50$)) nanoparticles, such as Cu, Cu_{50}Ag , Cu_{20}Ag , Cu_{10}Ag , Cu_5Ag , CuAg, CuAg_2 , and Ag, by using $\text{Cu}(\text{CH}_3\text{COO})_2$ and AgNO_3 as the precursors. The samples were characterized by X-ray diffraction, transmission electron microscopy, thermogravimetric analysis, and X-ray photoelectron spectroscopy. The Cu_xAg hybrid nanostructure showed good particle dispersion, and Cu and Ag metals were well mixed. The catalytic properties of these bimetallic Cu_xAg nanoparticles as model catalysts for the Rochow reaction were explored. Compared to monometallic Cu and Ag nanoparticles, bimetallic Cu_xAg nanoparticles resulted in a much higher silicon conversion, which is attributed to the synergistic electronic effect between Cu and Ag metals. For example, the Cu atom was observed to have a lower electron density in the Cu_xAg bimetallic nanoparticle than that in monometallic Cu nanoparticles, which enhanced the formation of methylchlorosilanes on the silicon surface with chloromethane, demonstrating the significance of the Cu_xAg bimetallic catalysts in catalytic reactions during organosilane synthesis. The insights gained in this study should be conducive to the design of good Cu-based catalysts for the Rochow reaction.

Received 16th March 2015

Accepted 16th June 2015

DOI: 10.1039/c5ra04575d

www.rsc.org/advances

1. Introduction

Recently, the fabrication of bimetallic nanoparticles has been of great interest because of the ample opportunities provided to modify and enhance their optical and electronic properties *via* engineering of the particle composition, structure and even geometric morphology.^{1–8} Many bimetallic nanoparticles, such as AuCu,⁹ AgCu,¹⁰ RuCu,¹¹ PdCu,¹² PtCu,¹³ FeCu,¹⁴ NiCu,¹⁵ PdAu,¹⁶ PtPd,¹⁷ PdRu,¹⁸ PtCo,¹⁹ and PtNi²⁰ have been applied in aerobic oxidation,⁹ the oxygen reduction reaction,^{10,20} hydrogenation,^{11,16} the Sonogashira reaction,¹² oxidation of formic acid,¹³ degradation of organic contaminants,¹⁴ hydrogen production,¹⁵ ethanol electro-oxidation,¹⁷ methanol electro-oxidation,¹⁸ and hydrogenolysis.¹⁹ In particular, several reports revealed that Cu-based bimetallic catalysts exhibited much higher activity than monometallic Cu particles in catalytic reactions, *e.g.*, CuAu improved the reduction of carbon dioxide,¹ CuPd enhanced the oxidation of cyclohexane by hydrogen peroxide,²¹ CuAg enhanced the oxidation of methanol to CO_2 ,²²

and CuRu lowered the activation energy for the hydrolytic dehydrogenation of ammonia borane,²³ *etc.*

Rochow reaction was discovered in 1940s as the direct synthesis route to produce methylchlorosilanes *via* the reaction of silicon (Si) with chloromethane on Cu-based catalysts.²⁴ Over the past few decades, many researches have indicated that the Cu-based catalysts are the main catalysts applicable to Rochow reaction,^{25–28} and Zn and ZnO are effective in promoting the Cu-based catalyst by increasing the dimethyldichlorosilane selectivity and Si conversion.^{29,30} In general, the Cu-based catalysts are mixed with Zn or ZnO promoters both in the organosilane industry and in fundamental studies. In the past five years, our group has studied the Cu,³¹ Cu_2O ,^{32,33} $\text{Cu@Cu}_2\text{O}$,³⁴ CuO ,^{35,36} $\text{Cu-Cu}_2\text{O-CuO}$ composites,^{37,38} and CuCl ³⁹ as active components for this reaction, and found that the catalyst composition, structure, size, and shape have significant effect on it. However, the above catalysts still suffer from low Si conversion, limiting their practical application. Because of the presence of the synergistic effect in some bimetallic catalysts,^{22,40} and the vast opportunities for engineering the particle composition, size and shape, *etc.*, it is expected that the bimetallic catalysts may have high potentiality for Rochow reaction.^{1,41}

Herein, we synthesize the bimetallic Cu_xAg ($0 \leq x \leq 50$) nanoparticles *via* a oleylamine thermal reduction process using $\text{Cu}(\text{CH}_3\text{COO})_2$ and AgNO_3 as the precursors. The composite of Cu_xAg nanoparticles can be easily controlled by adjusting the ratio of metal precursors. These bimetallic Cu_xAg (such as

^aState Key Laboratory of Multiphase Complex Systems, Institute of Process Engineering, Chinese Academy of Sciences, Beijing, China 100190. E-mail: zhangzl@ipe.ac.cn; fbsu@ipe.ac.cn; Fax: +86-10-82544851; Tel: +86-10-82544850

^bInstitute of Chemical Engineering and Sciences, A*star, 1 Pesek Road, Jurong Island, Singapore 627833

† Electronic supplementary information (ESI) available. See DOI: 10.1039/c5ra04575d

Cu₅₀Ag, Cu₂₀Ag, Cu₁₀Ag, Cu₅Ag, CuAg, and CuAg₂) nanoparticles are used as model catalysts for Rochow reaction. Compared with the Si conversion for monometallic Cu (35.4% for Cu) and Ag (0% for Ag) nanoparticles, these bimetallic Cu_xAg nanoparticles exhibit much enhanced Si conversion (65.4% for Cu₅₀Ag, 68.6% for Cu₂₀Ag, 71.1% for Cu₁₀Ag, 73.0% for Cu₅Ag, and 70.3% for CuAg), demonstrating the synergistic electronic effect between Cu and Ag atoms in the AgCu bimetallic nanoparticles, which led to the lower electron density for Cu atoms, in the Rochow reaction. This work provides useful clues for improving the Cu-based catalysts to achieve higher Si conversion in Rochow reaction.

2. Experimental

2.1. Synthesis of Cu_xAg (0 ≤ x ≤ 50) nanoparticles

A modified thermal decomposition process was used to synthesize the Cu_xAg bimetallic nanoparticles. AgNO₃ (A.R., Sinopharm Chemical Reagent Co., Ltd, China) was used as the Ag precursor, Cu(CH₃COO)₂ (A.R., Sinopharm Chemical Reagent Co., Ltd, China) as the Cu precursor, and oleylamine (C₁₈H₃₇N, Sigma-Aldrich) as the solvent, surfactant and reducing agent.^{42,43} All chemicals were used as received without further purification. In a typical synthesis for CuAg nanoparticles, 10 mmol of Cu(CH₃COO)₂ and 10 mmol of AgNO₃ were added to 80 mL of oleylamine in a three neck flask, which was then heated to 180 °C for 8 h with stirring. The nanoparticles were washed with ethanol (A.R., Sinopharm Chemical Reagent Co., Ltd, China) and hexamethylene (A.R., Sinopharm Chemical Reagent Co., Ltd, China), and separated by several rounds of centrifugation. The purified nanoparticles were then dried at 60 °C for more than 24 h in a vacuum oven. Similarly, Cu, Cu₅₀Ag, Cu₂₀Ag, Cu₁₀Ag, Cu₅Ag, CuAg₂, and Ag nanoparticles were prepared by varying the ratio of Cu and Ag precursors. Meanwhile, Cu–Ag composites were prepared as a comparison in the following way: 10 mmol of Cu(CH₃COO)₂ was added to 80 mL of oleylamine in a three-neck flask, which was then heated to 180 °C for 8 h with stirring. Subsequently, 10 mmol of AgNO₃ was added to the three-neck flask and the solution was stirred for another 8 h. The nanoparticles were washed with ethanol and hexamethylene *via* centrifugation, and dried in a vacuum oven at 60 °C for 24 h. In addition, Cu + Ag composites were prepared by mixing the same weight of Cu nanoparticles and Ag nanoparticles.

2.2. Materials characterization

X-ray diffraction patterns (XRD) were recorded on a PANalytical X'Pert PRO MPD using the Cu K α radiation ($\lambda = 1.5418 \text{ \AA}$). The microscopic feature of the samples was characterized by field-emission scanning electron microscopy (FESEM) with an energy-dispersive X-ray spectrometer (EDX) (JSM-7001F, JEOL, Tokyo, Japan) and transmission electron microscopy (TEM) with an EDX (JEM-2010F, JEOL, Tokyo, Japan) operated at 300 kV. Thermogravimetric (TG) analysis was carried out on an EXSTAR TG/DTA 6300 (Seiko Instruments, Japan) at a heating rate of 2 °C min⁻¹ in air. X-ray photoelectron spectroscopy (XPS)

analysis was carried out on an ESCALAB 250Xi from Thermo Scientific Corporation using Al_{K α} X-ray radiation. The amount of carbon deposited was measured using a CS-344 Infrared Analyzer (Leco, US).

2.3. Catalytic measurement

The evaluation of catalysts was carried out with a typical lab fixed-bed reactor.³² The prepared Cu_xAg catalysts were thermal treatment at 350 °C before the catalytic reaction. The Si powder (20–50 mesh) and prepared Cu_xAg catalyst together with Zn as a promoter with a ratio of 200 : 10 : 1 were mixed homogeneously to form a contact mass, which was loaded in the glass reactor. The reactor system was purged with purified N₂ for 0.5 h followed by heating to 325 °C within 1 h under a N₂ flow rate of 25 mL min⁻¹. Subsequently, N₂ was turned off, and CH₃Cl with a flow rate of 25 mL min⁻¹ was introduced into the reactor to react with Si followed by heating to 325 °C. After a given period of 24 h, the reaction was stopped. The gas product was cooled into a liquid phase with the circulator bath controlled at –5 °C by a programmable thermal circulator (Ningbo Xinzhi biological technology Co., LTD). The waste contact mass (solid residue after reaction), containing unreacted Si powder, Cu, Ag, and Zn compounds were weighed for calculating Si conversion. The products in the liquid solution were quantitative analyzed on an Agilent Technologies (GC-7890A) gas chromatograph equipped with KB-201 column and TCD detector. Gas chromatography system was used for identification of the products, which was mainly comprised of methyltrichlorosilane (CH₃SiCl₃, M1), dimethyldichlorosilane ((CH₃)₂SiCl₂, M2), trimethylchlorosilane ((CH₃)₃SiCl, M3), methyldichlorosilane (CH₃SiHCl₂, M1H), dimethylchlorosilane ((CH₃)₂SiHCl, M2H), low boiler (LB) and high boiler (HB). The selectivity of the products was calculated by the peak area ratio (in percentage). The Si conversion was that the ratio of weight difference of contact mass (before and after reaction) and weight of Si (before reaction) (formula (1)).

Conversion of Si (C_{Si}) =

$$\frac{\text{weight}_{\text{contact mass before reaction}} - \text{weight}_{\text{contact mass after reaction}}}{\text{weight}_{\text{Si before reaction}}} \times 100\% \quad (1)$$

3. Results and discussion

3.1. Catalyst characterization

3.1.1. XRD analysis. Fig. 1 shows the XRD results of the synthesized Cu_xAg (0 ≤ x ≤ 50) nanoparticles obtained by adding different ratio of Cu(CH₃COO)₂ and AgNO₃ precursors. For the sample Cu obtained after only adding Cu(CH₃COO)₂ precursor, diffraction peaks at 2 θ values of 43.5, 50.7, and 74.4° are observed, which are corresponded to the lattice planes of (111), (200), and (220) for Cu phase (JCPDS card no. 70-3039).⁴³ When the AgNO₃ precursor is added, besides the above Cu diffraction peaks, several other peaks at 2 θ values of 38.5, 44.5, 64.7, 77.7, and 81.9°, which correspond to the lattice planes of (111), (200), (220), (311), and (222) of Ag phase (JCPDS card no. 04-0783),⁴⁴ are also observed, suggesting that samples of

Cu₅₀Ag, Cu₂₀Ag, Cu₁₀Ag, Cu₅Ag, CuAg, and CuAg₂ are composed of both Cu and Ag phases. When the AgNO₃ precursor is simply added, the pure monometallic Ag nanoparticles are prepared. No other obvious crystalline impurities can be observed for these samples. Calculated over the (111) reflection using the classical Scherrer equation, the average crystallite diameters for Cu and Ag samples are 45.6 and 12.5 nm, respectively, suggesting that the Ag nanoparticles have a smaller crystallite size than Cu nanoparticles. In addition, the average crystallite diameters for Cu and Ag crystallites in Cu₅₀Ag, Cu₂₀Ag, Cu₁₀Ag, Cu₅Ag, CuAg, and CuAg₂ bimetallic nanoparticles are 43.2 and 8.5 nm, 38.6 and 8.9 nm, 29.5 and 9.6 nm, 21.7 and 10.2 nm, 18.6 and 11.5 nm, 15.6 and 12.0 nm, respectively, indicating that the average diameter of Cu crystallite is decreasing and Ag crystallite is increasing with the rising amount of Ag.

3.1.2. SEM and TEM characterization. Fig. 2a shows the transmission electron microscopy (TEM) image of CuAg nanoparticles. The nanoparticles in the white box have a mean size of 12.2 nm and standard deviations of 2.1. The high-resolution TEM (HRTEM) image of the CuAg nanoparticles in Fig. 2b shows that Cu has a spacing distance of 0.21 nm, which corresponds to the interplanar distance of the (111) plane of the Cu, while the lattice fringe spacing of 0.24 nm corresponds to the lattice fringe distance of the (111) plane in Ag. To further confirm the bimetallic structure and the composition of the CuAg nanoparticles, TEM-EDX image (Fig. 2c), line scan (Fig. 2d), and TEM-EDX analysis (inset of Fig. 2c) are also carried out. The line scan (Fig. 2d) along the direction denoted by the white line in Fig. 2c shows that Cu and Ag are mixed well in the nanoparticles. The TEM-EDX spectrum of CuAg nanoparticles shown in inset of Fig. 2c demonstrates the presence of Cu and Ag elements with an approximate atomic ratio of 1 : 1. TEM image of Fig. S1a† shows that no obvious Ag nanoparticles are

attached on the surface of Cu nanoparticles for Cu₅₀-Ag nanoparticles after only adding 0.2 mmol AgNO₃ precursor. When the AgNO₃ precursor amount is increased to 0.5 mmol and 1.0 mmol, small Ag nanoparticles are attached on the surface of Cu nanoparticles for Cu₂₀-Ag (Fig. S1b†) and Cu₁₀-Ag (Fig. S1c†). With increase of the AgNO₃ precursor amount to 2.0 mmol (Fig. S1d†), large Ag nanoparticles are attached on the surface of Cu nanoparticles. With further increase of the AgNO₃ precursor amount to 10.0 mmol, the TEM image of Cu-Ag nanoparticles in Fig. 2e reveals that the larger Ag nanoparticles are highly dispersed on the surface of the large Cu nanoparticles. The atomic ratio of Cu : Ag is also about 1 : 1 from the TEM-EDX spectrum of Cu-Ag nanoparticles (Fig. 2f). In addition, the SEM image of Cu-Ag₂ nanoparticles indicates Cu and Ag nanoparticles are aggregated together (not shown here). In the preparation processes, the Cu nanoparticles act as a spacer separating the Ag nanoparticles, and the size of Ag nanoparticles is increasing with the rising amount of AgNO₃ precursor. In case with fixed amount of Cu nanoparticles, it will have the fixed adsorption sites for the given amounts of Cu nanoparticles. After adding less amount of AgNO₃ precursor, the formed Ag nanoparticles with smaller in size are attached on the fixed adsorption sites of Cu nanoparticles. Upon further adding more AgNO₃ precursor, the formed smaller Ag nanoparticles can grow larger with the addition AgNO₃ precursor.

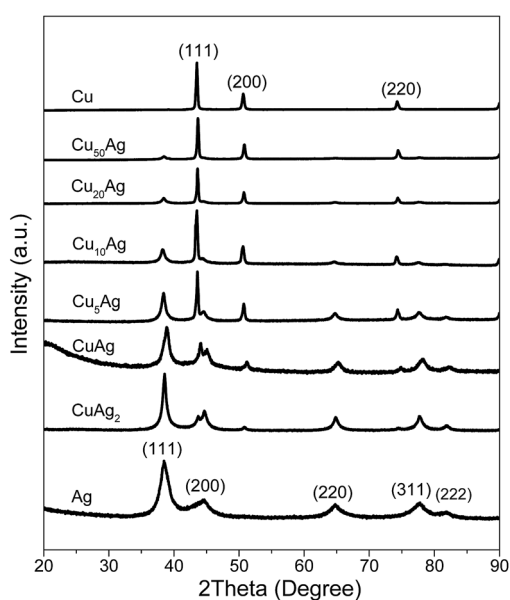


Fig. 1 XRD patterns for samples Cu, Cu₅₀Ag, Cu₂₀Ag, Cu₁₀Ag, Cu₅Ag, CuAg, CuAg₂, and Ag nanoparticles.

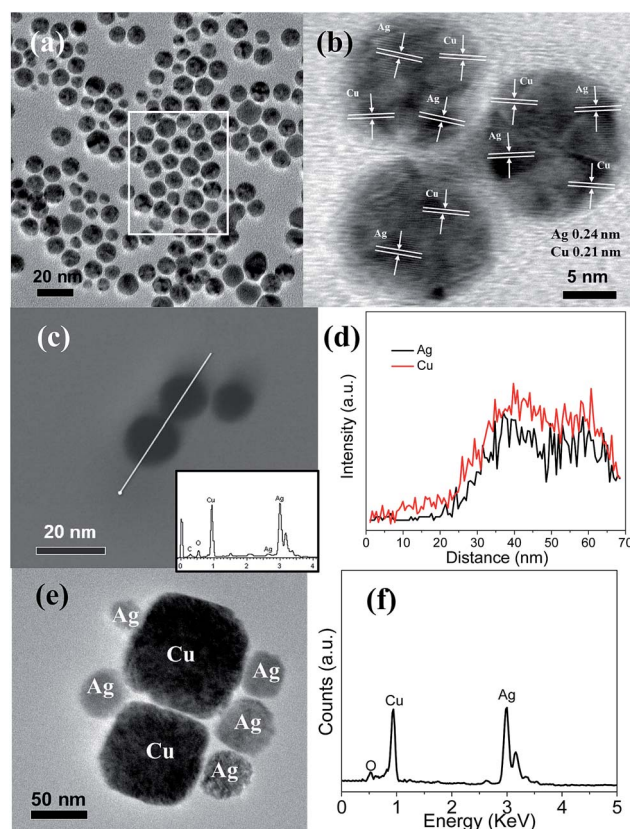


Fig. 2 TEM (a), HRTEM (b), and TEM-EDX images (c) (inset is its EDX spectrum), the line scan along the white line in (c) (d), TEM image (e) and its TEM-EDX spectrum (f) of Cu-Ag nanoparticles.

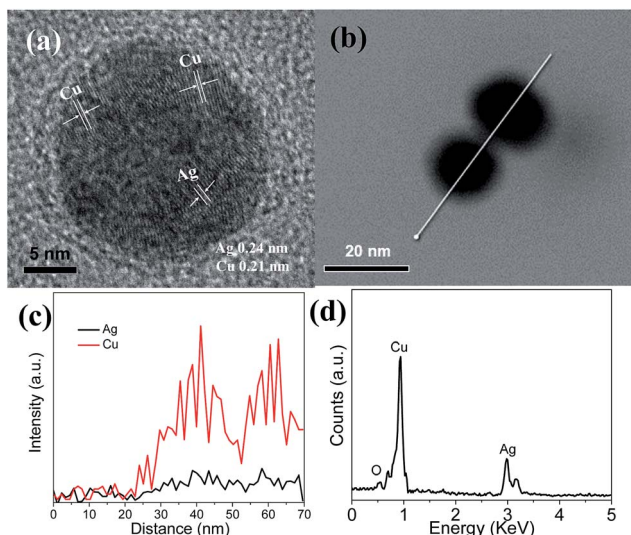


Fig. 3 HRTEM image (a), TEM-EDX image (b), the line scan along the direction denoted by the white line in (b) (c), and its TEM-EDX spectrum (d) of Cu₅Ag nanoparticles.

A similar morphology is observed for Cu₅Ag nanoparticles. The HRTEM image of Cu₅Ag nanoparticles shown in Fig. 3a indicates that Cu and Ag have a spacing distance of about 0.21 nm and 0.24 nm, respectively, corresponding to the interplanar distance of the (111) plane of the Cu and Ag phases. The line scan (Fig. 3c) along the white line in Fig. 3b also shows that Cu and Ag are mixed fairly in the nanoparticles. Fig. 3d reveals the TEM-EDX spectrum of Cu₅Ag, indicating the presence of Cu and Ag elements with an approximate atomic ratio of 5 : 1, consistent with the initial atomic ratio of Cu(CH₃COO)₂ and AgNO₃ precursors.

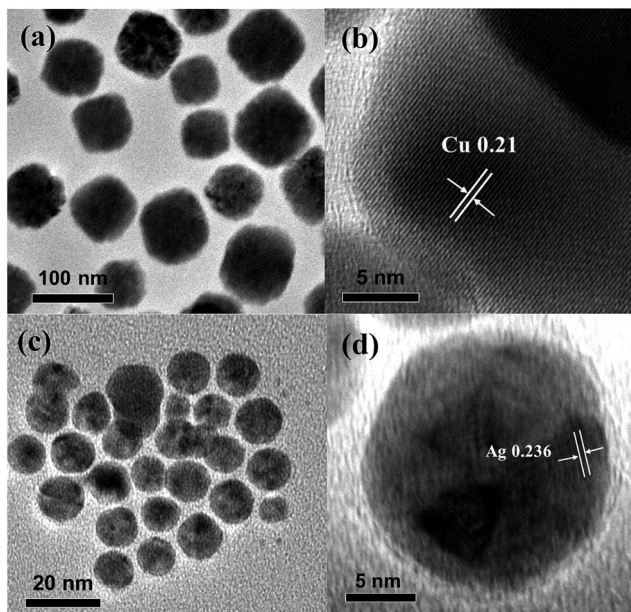


Fig. 4 TEM (a) and HRTEM (b) images of pure monometallic Cu nanoparticles, and TEM (c) and HRTEM (d) images of pure monometallic Ag nanoparticles.

The TEM image of Fig. 4a shows that Cu nanoparticles with a mean size of 73.6 nm and a standard deviation of 8.2 are synthesized after addition of Cu(CH₃COO)₂ precursor only. The HRTEM image in Fig. 4b indicates a spacing distance of 0.21 nm for these Cu nanoparticles, which corresponds to the interplanar distance of the (111) plane. After addition of 0.2 mmol, 0.5 mmol, and 1.0 mmol AgNO₃ precursor together, the obtained Cu₅₀Ag (Fig. S1a[†]), Cu₂₀Ag (Fig. S1b[†]), and Cu₁₀Ag (Fig. S1c[†]) nanoparticles have the similar size of pure Cu nanoparticles (Fig. 4a). However, upon further increasing the AgNO₃ precursor amount to 5.0 mmol, 10.0 mmol, and 20.0 mmol, it is clearly seen that the size of Cu₅Ag (Fig. 3a), CuAg (Fig. 2a), and CuAg₂ (Fig. S1d[†]) nanoparticles are similar to the pure Ag nanoparticles (Fig. 4c). Compared with Cu (Fig. 4a), Cu₅₀Ag (Fig. S1a[†]), Cu₂₀Ag (Fig. S1b[†]), and Cu₁₀Ag (Fig. S1c[†]) nanoparticles, the prepared Cu₅Ag (Fig. 3a), CuAg (Fig. 2a), CuAg₂ (Fig. S1d[†]), and Ag (Fig. 4c) nanoparticles are smaller in size, consistent with the above XRD calculated results using the classical Scherrer equation. Fig. 4d indicates that the lattice fringe spacing of Ag is about 0.24 nm, corresponding to the interplanar distance of the (111) plane. But we failed to obtain a clear HRTEM image, probably because of the surface covering of the smaller Ag nanoparticles by oleylamine.⁴⁵

3.1.3. XPS and TG analysis. We further characterized the structure and composition of the Cu, Ag, and Cu_xAg nanoparticles by Thermogravimetric (TG) and X-ray photoelectron spectroscopy (XPS) analysis. Fig. 5a shows that, for CuAg nanoparticles, the Cu 2p spectrum has one strong peak at 932.8 eV for Cu 2p_{3/2}, which is close to that of Cu⁰ or Cu⁺, but quite far away from that of Cu²⁺ (934.1 eV).⁴⁶ However, two peaks at 932.6 eV and 934.6 eV are observed for pure Cu nanoparticles. These peaks can be attributed to Cu⁰ or Cu⁺, and Cu²⁺, respectively, suggesting that pure Cu nanoparticles are more easily oxidized than Cu in CuAg nanoparticles without any deliberate oxidation treatments. In the Ag 3d spectrum shown in Fig. 5b, the strong peak at 368.2 eV is assigned to Ag 3d_{5/2} for CuAg nanoparticles,

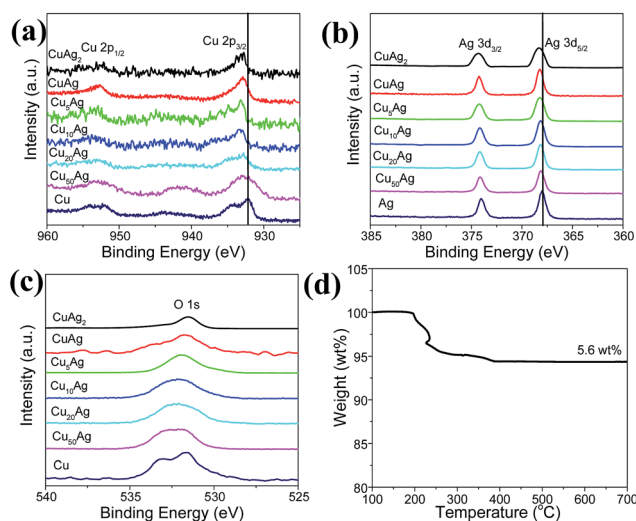


Fig. 5 XPS spectra for all the samples: Cu 2p (a), Ag 3d (b), and O 1s (c), and TG curve for CuAg nanoparticles in air (d).

and 368.0 eV to Ag 3d_{5/2} for pure Ag nanoparticles, indicating the metallic nature of Ag in CuAg nanoparticles,⁴⁷ consistent with the above XRD analysis.

In addition, compared with the pure Cu and Ag nanoparticles, a peak shift is observed for bimetallic nanoparticles. Ag has a higher redox potential than Cu, thus the former has strong attraction than Cu for the electron in the Cu_xAg bimetallic nanoparticles, leading to lower electron densities of Cu atoms in the Cu_xAg bimetallic nanoparticles than those in the pure Cu nanoparticles. Indeed, from Mulliken charge analysis, the atomic charge of Cu in the Cu_xAg bimetallic nanoparticle has a positive value.⁴⁸ The peak shift in the XPS analysis clearly shows the lower electron density of Cu in the Cu_xAg bimetallic nanoparticle than that of pure Cu nanoparticles, suggesting the electronic interaction between the Ag and Cu.⁴⁹ The increase of binding energy of Cu 2p_{3/2} and Cu 2p_{1/2} in Cu_xAg bimetallic nanoparticles (Fig. 5a) indicates the electron transfer from Cu to Ag, which may due to the size and the ratio of Cu : Ag in the Cu_xAg bimetallic nanoparticles. The peak increase for Ag 3d_{5/2} and Ag 3d_{3/2} in bimetallic samples (Fig. 5b) is caused by the strong attraction for electron by Ag than Cu. This can be attributed to the synergistic electronic effect between Cu and Ag. Fig. 5c displays the O1s spectra of the samples. There is one peak for bimetallic nanoparticle, and a relative strong peak for pure Cu nanoparticles at 531.7 eV, which can be ascribed to copper oxide species due to the partial oxidation of the Cu nanoparticles on the surface, further confirming that pure Cu nanoparticles are more susceptible to oxidation than Cu in Cu_xAg nanoparticles. In addition, the atomic ratio of Cu and Ag elements is also approximately 1 : 1 from XPS analysis. Fig. 5d shows the TG curve for CuAg nanoparticles in air, the weight loss of about 5.6 wt% may be derived from the trace amount of organic residue on their surface. However, there is no further weight increase for CuAg nanoparticles in air at higher temperatures, probably because of formation of the CuAg alloy, which is more resistant to oxidation even annealed them in air at higher temperatures.

3.2. Formation process of Cu_xAg (0 ≤ x ≤ 50) nanoparticles

The possible formation process of the Cu_xAg (0 ≤ x ≤ 50) nanoparticles is proposed according to the above XRD, TEM and XPS analysis, and is illustrated in Fig. 6. In the first stage, the Cu²⁺ and Ag²⁺ ions are reduced and nucleated to form Cu and Ag nanoclusters under solvothermal conditions with assistance of oleylamine (C₁₈H₃₇N), which acts as the solvent, surfactant as well as the reducing agent.^{42,43} In one control experiment, we also synthesized isolated Cu and Ag

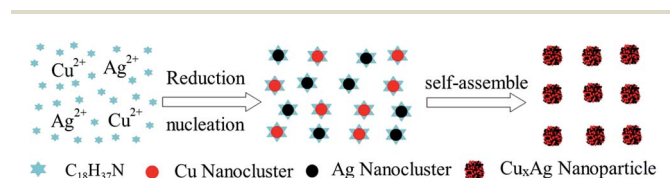


Fig. 6 The illustration of the formation process for Cu_xAg (0 ≤ x ≤ 50) nanoparticles.

nanoparticles with a size range of about 1–5 nm at 180 °C by shortening the reaction time to 1.5 h (Fig. S3[†]), in which, the Ag and Cu particles were still not fused together. Furthermore, in another control experiment, we synthesized Cu–Ag sample (Fig. 2g) by adding and reducing Cu and Ag separately. Interestingly, the individual Cu and Ag particles were observed but they formed loosely combined assemblies (Fig. 2e). Obviously, C₁₈H₃₇N can be absorbed on the surface of the Cu and Ag nanoclusters and act as structure-directing agents to regulate their surface state, influence the nucleation and aggregation process of these nanoclusters, which are finally self-assembled to the Cu_xAg hybrid nanoparticles.

3.3. Catalytic property

Fig. 7 and Table 1 reveal the catalytic performance of Cu, Ag, Cu_xAg bimetallic nanoparticles and commercial catalysts for Rochow reaction. It can be seen that much higher Si conversion are observed on Cu₅₀Ag (65.4%), Cu₂₀Ag (68.6%), Cu₁₀Ag (71.1%), Cu₅Ag (73.0%), CuAg (70.3%), and CuAg₂ (50.4%) than that on the Cu nanoparticles (35.4%), Ag nanoparticles (0%) and on the several reported Cu-based catalysts (Table 2), which should be related to the synergistic electronic effect between the Cu and Ag nanoparticles with electron transfer from Cu to Ag. The Si conversion is first increased with the increase of Ag content (Cu/Ag from 1 : 0 to 5 : 1), but decreased again with further increase of Ag content. It is understandable that the addition of excess Ag will lead to the final decrease of the Si conversion, as it is Cu, not Ag, that acts as the active sites. This can be evidenced in Table 1, the pure Ag has no activity in conversion of Si while the pure Cu works well for it. In addition, the top Si conversion are observed on Cu₁₀Ag (71.1%) and CuAg (70.6%), which are obviously higher than that on Cu₁₀–Ag (60.6%), Cu–Ag (57.6%), and Cu + Ag (48.2%), possibly because the Cu₁₀Ag and CuAg nanoparticles have more proper synergistic electronic interaction and local structure for Rochow reaction than that of Cu₁₀–Ag, Cu–Ag nanoparticles and Cu + Ag composites, although the details are still not clear. Comparing

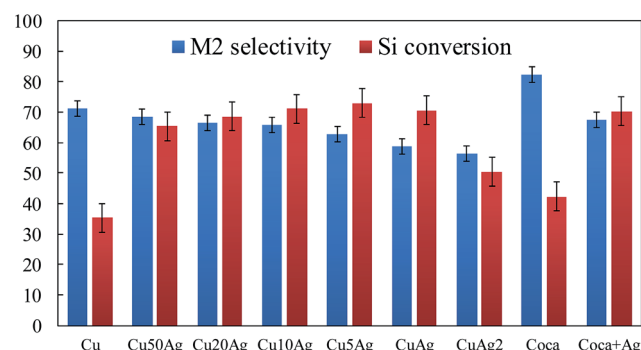


Fig. 7 Selectivity of dimethyldichlorosilane (M2) and conversion of Si for Cu, Ag, Cu_xAg bimetallic nanoparticles and commercial catalysts (named Coca) for Rochow reaction. Error bars, standard deviation of triplicated wells. The catalytic measurements were independently repeated three times to obtain three M2 selectivity and Si conversion for each catalyst.

with pure Cu nanoparticles, the CuAg samples always have higher Si conversion but lower M2 selectivity. Similar phenomenon is observed for the commercial catalyst. After adding Ag nanoparticles, it shows a much higher Si conversion of 70.2%, a lower M2 of 72.6%, as compared with that of the commercial catalyst without adding Ag nanoparticles (42.3% and 82.3% respectively), indicating the importance of the Ag in the Cu-based catalyst. Since the high similarity in particle size in the prepared Cu_xAg and the commercial catalyst without Ag nanoparticles or added with Ag nanoparticles, the particle sizes of catalyst should not be the main reason for the difference in Si conversion. In other words, the structural factors such as the synergistic electronic effect of the Cu_xAg catalysts (Ag has a higher redox potential than Cu, and has strong attraction than Cu for the electron, leading to lower electron densities of Cu atoms in the Cu_xAg bimetallic nanoparticles) should have more important role for this catalytic reaction. As dimethyldichlorosilane (M2) is the

Table 1 Catalytic performance of Cu, Ag, Cu_xAg bimetallic nanoparticles and commercial catalysts (named Coca)

| Sample | Product composition (%) | | | | | | | C_{Si} (%) |
|----------------------------|-------------------------|------|-----|-----|-----|-----|-----|---------------------|
| | M1 | M2 | M3 | M1H | M2H | LB | HB | |
| Cu | 18.3 | 71.3 | 2.8 | 2.7 | 1.1 | 0.1 | 3.7 | 35.4 |
| Cu_{50}Ag | 19.4 | 68.4 | 2.1 | 6.4 | 0.9 | 0.2 | 2.6 | 65.4 |
| Cu_{20}Ag | 20.8 | 66.5 | 2.2 | 6.5 | 0.8 | 0.2 | 3.0 | 68.6 |
| Cu_{10}Ag | 22.4 | 65.9 | 1.9 | 6.9 | 0.8 | 0.1 | 2.0 | 71.1 |
| $\text{Cu}_{10}\text{-Ag}$ | 25.4 | 60.4 | 2.1 | 6.7 | 1.9 | 0.2 | 3.3 | 60.6 |
| Cu_5Ag | 24.9 | 62.6 | 1.9 | 6.3 | 0.8 | 0.5 | 3.0 | 73.0 |
| CuAg | 28.3 | 58.6 | 2.0 | 6.9 | 0.8 | 0.3 | 3.1 | 70.6 |
| Cu-Ag | 33.2 | 52.4 | 2.1 | 6.7 | 1.9 | 0.2 | 3.5 | 57.6 |
| Cu + Ag | 30.3 | 56.9 | 2.0 | 6.4 | 1.2 | 0.2 | 3.0 | 48.2 |
| CuAg_2 | 28.9 | 56.4 | 2.1 | 6.8 | 0.9 | 0.4 | 4.5 | 50.4 |
| Ag | 0 | 0 | 0 | 0 | 0 | 0 | 0 | 0 |
| Coca | 12.2 | 82.3 | 2.4 | 0.1 | 0.2 | 0.4 | 2.4 | 42.3 |
| Coca + Ag | 19.7 | 72.6 | 2.6 | 0.1 | 0.2 | 2.5 | 2.3 | 70.2 |

Table 2 A comparison of the Si conversion for Cu_xAg catalysts with several reported Cu-based catalyst^a

| Sample | C_{Si} (%) | Ref. |
|---|---------------------|-----------|
| Cu_5Ag nanoparticles | 73.0 | This work |
| CuAg nanoparticles | 70.6 | This work |
| Porous Cu microparticles | 33.5 | 31 |
| Mesoporous Cu_2O microspheres | 33.2 | 32 |
| Hexahedron Cu_2O microparticles | 40.4 | 33 |
| Core-shell $\text{Cu}@\text{Cu}_2\text{O}$ microspheres | 29.2 | 34 |
| Flower-like CuO microparticles | 38.8 | 35 |
| Dandelion-like CuO microparticles | 41.6 | 36 |
| $\text{CuO-Cu}_2\text{O-Cu}$ nanoparticles | 23.4 | 37 |
| $\text{Cu-Cu}_2\text{O-CuO}$ microparticles | 32.4 | 38 |
| Tetrahedra CuCl microparticles | 24.8 | 39 |
| CuCl particles | ~12 | 50 |
| CuCl particles | ~20 | 29 |

^a Ref. 29 Si : catalyst : Zn = 200 : 10 : 1, temperature 300 °C; ref. 31–39 Si : catalyst : Zn = 100 : 10 : 1, temperature 325 °C; ref. 50 Si : catalyst : Zn = 100 : 10 : 0.06, temperature 300 °C; this work Si : catalyst : Zn = 200 : 10 : 1, temperature 325 °C.

most valuable precursor in organosilane industry, and the bimetallic Cu_xAg nanoparticles and commercial catalyst added with Ag nanoparticles always have lower selectivity of M2 than their counterparts without Ag. In the design of Rochow reaction catalysts, it should carefully balance the Si conversion and M2 selectivity by adjusting the ratio of Cu and Ag.

The compositions of contact masses including the deposited carbon after reaction with Cu and CuAg catalyst were further characterized by XRD, SEM, SEM-EDX. Fig. 8 displays XRD patterns of the contact masses after reaction with Cu and CuAg catalyst, in which the unreacted Si, Cu, and Ag phases with CuAg catalyst, and the unreacted Si, and Cu phases with Cu catalyst are detected. In Rochow reaction, Cu_xSi is normally suggested as the key catalytic active species, from which M2 is produced.^{51,52} Cu_xSi formed between Cu-based catalyst and Si interface is an indicator of the Cu-based catalyst activity.⁵³ When Cu-based catalyst and Si are brought together at elevated temperatures, Cu_xSi is formed, from which methylchlorosilanes can be produced. In addition of Cu, Ag, and Si peaks, a small peak of Cu_xSi is observed in the XRD patterns of the reacted contact masses with CuAg catalyst, suggesting that the bimetallic CuAg nanoparticles are more active in generating Cu_xSi active species. We also found there is a shorter induction period for bimetallic CuAg nanoparticles (about 2 h) as compared to the monometallic Cu nanoparticles (about 10 h), possibly because of the higher activity of the bimetallic CuAg nanoparticles.

The scanning electron microscopy (SEM) and SEM-EDX analysis results for the contact masses after reaction with Cu and CuAg catalysts are shown in Fig. 9. Fig. 9a reveals the SEM image of the reacted contact mass with Cu catalyst, in which a large number of deposited carbon fibers are formed. The EDX spectrum (Fig. 9b) demonstrates that the contact mass after the reaction mainly consists of C, O, Si, and Cu, of which C and Si atoms are the most predominant. However, SEM image

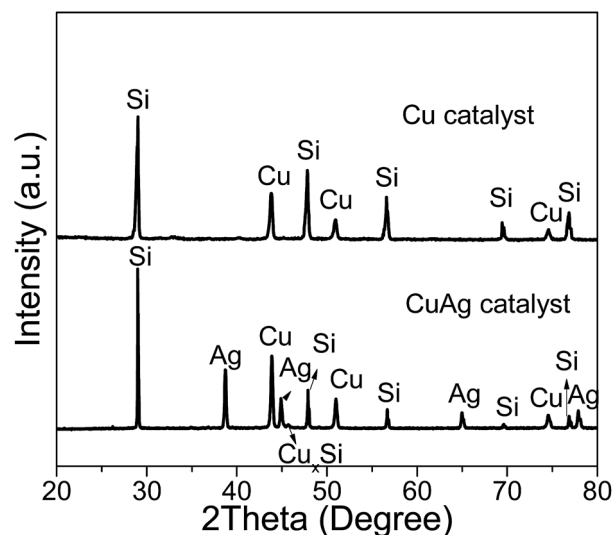


Fig. 8 XRD patterns of the contact masses after reaction with Cu and CuAg catalyst.

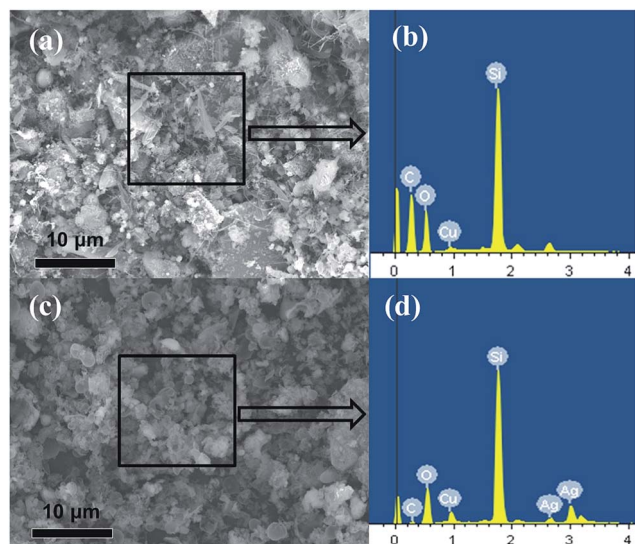


Fig. 9 SEM images (a and c), and their EDX spectrum (b and d) of the contact masses after reaction for Cu catalyst (a and b), and CuAg catalyst (c and d).

(Fig. 9c) and its EDX spectrum (Fig. 9d) of the reacted contact mass with CuAg catalyst shows it mainly consists of C, O, Si, Ag, and Cu, of which Si atoms are the major, and little C is observed. The formation of carbon deposit is due to the cleavage of the C–H and C–Cl bond in CH_3Cl monolayers on the surface of contact mass, which can restrain the catalytic reaction. The content of carbon deposited on the surface of the reacted contact masses is measured using a CS-344 Infrared Analyzer, which revealed that CuAg catalyst with Si contains 0.262 wt% of carbon, much lower than the value of 1.206 wt% on Cu catalyst with Si, consistent with the above SEM-EDX analysis, indicating that the CuAg catalyst improve the anti-coking ability.

4. Conclusions

In conclusion, we have demonstrated a thermal reduction process to prepare bimetallic Cu_xAg ($0 \leq x \leq 50$) nanoparticles. These Cu_xAg nanoparticles with various compositions have diameters in the range of 5–100 nm. For Rochow reaction, higher Si conversion are always observed on the bimetallic Cu_xAg nanoparticles (such as 65.4% for Cu_{50}Ag , 68.6% for Cu_{20}Ag , 71.1% for Cu_{10}Ag , 73.0% for Cu_5Ag , 70.3% for CuAg) than that on monometallic Cu nanoparticles (35.4%), which is due to the synergistic electronic effect between Cu and Ag, which enable the active sites to be more active for the formation of methylchlorosilanes on the Si surface with CH_3Cl . The highest Si conversion is observed on the Cu_{10}Ag and CuAg catalysts. However, it should be pointed out that, although there is a significant increase in Si conversion, the M2 selectivity is decreased after addition of the Ag component. The work sheds light on the development of more effective Cu-based catalysts for Rochow reaction.

Acknowledgements

The authors gratefully acknowledge the supports from the National Natural Science Foundation of China (no. 51402299 and 51272252) and Hundred Talents Program of the Chinese Academy of Sciences.

Notes and references

- 1 D. Kim, J. Resasco, Y. Yu, A. M. Asiri and P. D. Yang, *Nat. Commun.*, 2014, **5**, 4948.
- 2 A. M. Beale and B. M. Weckhuysen, *Phys. Chem. Chem. Phys.*, 2010, **12**, 5562.
- 3 P. Felfer, P. Benndorf, A. Masters, T. Maschmeyer and J. M. Cairney, *Angew. Chem., Int. Ed.*, 2014, **53**, 11190.
- 4 N. J. Divins, I. Angurell, C. Escudero, V. Perez-Dieste and J. Llorca, *Science*, 2014, **346**, 620.
- 5 U. Banin, *Nat. Mater.*, 2007, **6**, 625.
- 6 D. Asakura, C. H. Li, Y. Mizuno, M. Okubo, H. S. Zhou and D. R. Talham, *J. Am. Chem. Soc.*, 2013, **135**, 2793.
- 7 F. Studt, F. Abild-Pedersen, Q. X. Wu, A. D. Jensen, B. Temel, J. D. Grunwaldt and J. K. Norskov, *J. Catal.*, 2012, **293**, 51.
- 8 J. Yao, K. J. Koski, W. D. Luo, J. J. Cha, L. B. Hu, D. S. Kong, V. K. Narasimhan, K. F. Huo and Y. Cui, *Nat. Commun.*, 2014, **5**, 5670.
- 9 Y. Sugano, Y. Shiraishi, D. Tsukamoto, S. Ichikawa, S. Tanaka and T. Hirai, *Angew. Chem., Int. Ed.*, 2013, **52**, 5295.
- 10 K. Shin, D. H. Kim, S. C. Yeo and H. M. Lee, *Catal. Today*, 2012, **185**, 94.
- 11 J. J. Liu, L. L. Zhang, J. T. Zhang, T. Liu and X. S. Zhao, *Nanoscale*, 2013, **5**, 11044.
- 12 D. Sengupta, J. Saha, G. De and B. Basu, *J. Mater. Chem. A*, 2014, **2**, 3986.
- 13 S. Chen, H. Su, Y. Wang, W. Wu and J. Zeng, *Angew. Chem., Int. Ed.*, 2015, **54**, 108.
- 14 Y. B. Wang, H. Y. Zhao and G. H. Zhao, *Appl. Catal., B*, 2015, **164**, 396.
- 15 J. H. Lin and V. V. Gulians, *ChemCatChem*, 2012, **4**, 1611.
- 16 X. Yang, D. Chen, S. J. Liao, H. Y. Song, Y. W. Li, Z. Y. Fu and Y. L. Su, *J. Catal.*, 2012, **291**, 36.
- 17 X. Yang, Q. D. Yang, J. Xu and C. S. Lee, *J. Mater. Chem.*, 2012, **22**, 25492.
- 18 J. H. Zeng, F. B. Su, Y. F. Han, Z. Q. Tian, C. K. Poh, Z. L. Liu, J. Y. Lin, J. Y. Lee and X. S. Zhao, *J. Phys. Chem. C*, 2008, **112**, 15908.
- 19 G. H. Wang, J. Hilgert, F. H. Richter, F. Wang, H. J. Bongard, B. Spliethoff, C. Weidenthaler and F. Schuth, *Nat. Mater.*, 2014, **13**, 294.
- 20 C. L. Zhang, S. Y. Hwang, A. Trout and Z. M. Peng, *J. Am. Chem. Soc.*, 2014, **136**, 7805.
- 21 Z. Q. Zhang, J. L. Huang, L. Zhang, M. Sun, Y. C. Wang, Y. Lin and J. Zeng, *Nanotechnology*, 2014, **25**, 435602.
- 22 J. Czaplinska, I. Sobczak and M. Ziolek, *J. Phys. Chem. C*, 2014, **118**, 12796.
- 23 N. Cao, K. Hu, W. Luo and G. Z. Cheng, *J. Alloys Compd.*, 2014, **590**, 241.
- 24 E. G. Rochow, *J. Am. Chem. Soc.*, 1945, **67**, 963.

- 25 J. Acker and K. Bohmhammel, *J. Organomet. Chem.*, 2008, **693**, 2483.
- 26 R. Voorhoeve, B. Geertsem and J. C. Vlugter, *J. Catal.*, 1965, **4**, 43.
- 27 J. M. Bablin, A. C. Crawford, D. C. DeMoulied and L. N. Lewis, *Ind. Eng. Chem. Res.*, 2003, **42**, 3555.
- 28 W. Luo, G. Wang and J. Wang, *Ind. Eng. Chem. Res.*, 2006, **45**, 129.
- 29 L. N. Lewis and W. J. Ward, *Ind. Eng. Chem. Res.*, 2002, **41**, 397.
- 30 J. M. Bablin, A. C. Crawford, D. C. DeMoulied and L. N. Lewis, *Ind. Eng. Chem. Res.*, 2003, **42**, 3555.
- 31 Z. Zhang, H. Che, Y. Wang, X. She, J. Sun, P. Gunawan, Z. Zhong and F. Su, *ACS Appl. Mater. Interfaces*, 2012, **4**, 1295.
- 32 Z. Zhang, H. Che, Y. Wang, J. Gao, L. Zhao, X. She, J. Sun, P. Gunawan, Z. Zhong and F. Su, *Ind. Eng. Chem. Res.*, 2012, **51**, 1264.
- 33 Z. Zhang, H. Che, J. Gao, Y. Wang, X. She, J. Sun, P. Gunawan, Z. Zhong and F. Su, *Catal. Sci. Technol.*, 2012, **2**, 1207.
- 34 Z. Zhang, H. Che, Y. Wang, J. Gao, Y. Ping, Z. Zhong and F. Su, *Chem. Eng. J.*, 2012, **211**, 421.
- 35 Z. Zhang, H. Che, Y. Wang, J. Gao, X. She, J. Sun, Z. Zhong and F. Su, *RSC Adv.*, 2012, **2**, 2254.
- 36 Z. Zhang, H. Che, Y. Wang, L. Song, Z. Zhong and F. Su, *Catal. Sci. Technol.*, 2012, **2**, 1953.
- 37 W. Liu, L. Jia, Y. Wang, L. Song, Y. Zhu, X. Chen, Z. Zhong and F. Su, *Ind. Eng. Chem. Res.*, 2013, **52**, 6662.
- 38 S. Liu, Y. Wang, Y. Zhu, G. Wang, Z. Zhang, H. Che, L. Jia and F. Su, *RSC Adv.*, 2014, **4**, 7826.
- 39 X. Chen, L. Jia, Y. Wang, L. Song, Y. Zhu, W. Liu, Z. Zhong and F. Su, *J. Colloid Interface Sci.*, 2013, **404**, 16.
- 40 B. T. Meshesha, N. Barrabes, J. Llorca, A. Dafinov, F. Medina and K. Föttinger, *Appl. Catal., A*, 2013, **453**, 130.
- 41 W. L. Zhu, R. Michalsky, O. Metin, H. F. Lv, S. J. Guo, C. J. Wright, X. L. Sun, A. A. Peterson and S. H. Sun, *J. Am. Chem. Soc.*, 2013, **135**, 16833.
- 42 H. Hiramatsu and F. E. Osterloh, *Chem. Mater.*, 2004, **16**, 2509.
- 43 N. R. Kim, K. Shin, I. Jung, M. Shim and H. M. Lee, *J. Phys. Chem. C*, 2014, **118**, 26324.
- 44 W. X. Zhang, X. N. Yang, Q. Zhu, K. Wang, J. B. Lu, M. Chen and Z. H. Yang, *Ind. Eng. Chem. Res.*, 2014, **53**, 16316.
- 45 M. Chen, Y. G. Feng, X. Wang, T. C. Li, J. Y. Zhang and D. J. Qian, *Langmuir*, 2007, **23**, 5296.
- 46 C. K. Wu, M. Yin, S. O'Brien and J. T. Koberstein, *Chem. Mater.*, 2006, **18**, 6054.
- 47 E. Stathatos, P. Lianos, P. Falaras and A. Siokou, *Langmuir*, 2000, **16**, 2398.
- 48 R. S. Mulliken, *J. Chem. Phys.*, 1955, **23**, 1833.
- 49 Z. Chen, D. Mochizuki, M. M. Maitani and Y. Wada, *Nanotechnology*, 2013, **24**, 265602.
- 50 A. D. Gordon, B. J. Hinch and D. R. Strongin, *Catal. Lett.*, 2009, **133**, 14.
- 51 W. F. Banholzer and M. C. Burrell, *J. Catal.*, 1988, **114**, 259.
- 52 T. C. Frank, K. B. Kester and J. L. Falconer, *J. Catal.*, 1985, **91**, 44.
- 53 W. F. Banholzer, N. Lewis and W. Ward, *J. Catal.*, 1986, **101**, 405.